Applied Thermal Engineering 229 (2023) 120529

Contents lists available at ScienceDirect

Applied Thermal Engineering

journal homepage: www.elsevier.com/locate/ate

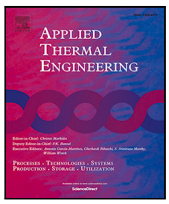

Research Paper

Thermal performance characteristics of a tessellated-impinging central receiver

D.J. Erasmus [a,*], A. Sánchez-González [b], M. Lubkoll [a], K.J. Craig [c], T.W. von Backström [a]

[a] Solar Thermal Energy Research Group (STERG), Department of Mechanical and Mechatronic Engineering, Stellenbosch University, Private Bag X1, Matieland 7602, South Africa

[b] Energy Systems Engineering Group (ISE), Department of Thermal and Fluid Engineering, Universidad Carlos III de Madrid, Av. Universidad, 30, 28911, Leganés, Madrid, Spain

[c] Department of Mechanical and Aeronautical Engineering, University of Pretoria, Pretoria 0002, South Africa

ARTICLE INFO

Keywords:
CSP
Central receiver
Pressurized air receiver

ABSTRACT

Current central receiver Concentrating Solar Power plants using molten salt as a heat transfer fluid add heat at around 565 °C in a power plant. Adding heat at a higher temperature can improve the thermodynamic performance and may reduce the cost of power. One way to achieve this is by using pressurized air solar receivers. Current receivers have achieved thermal efficiencies of around 80% at an outlet temperature of 800 °C. This paper investigates a novel central receiver technology that makes use of a tessellated array of heat transfer units. The units employ impingement heat transfer within a concave surface. The receiver can be scaled for a desired thermal rating by the number of heat transfer units. The convolution-projection flux modelling approach is used to model and project an incoming flux distribution on the receiver's surface. This flux distribution is interpreted by a Computational Fluid Dynamics model as a volumetric heat source. Radiative and convective heat losses are considered. An initial performance outlook estimates that an outlet temperature of 801 °C can be reached at a thermal efficiency of 59% and an exterior surface temperature of 1142 °C for an aperture flux of 635 kW/m^2. A limitation is an insufficient exterior surface area to absorb the incoming flux which causes a high surface temperature and thermal losses. Similar thermal performance is estimated at high and low pressures, with increased pumping losses at low pressures. The efficiency may be improved by taking advantage of a larger surface area relative to the aperture area.

1. Introduction

1.1. Background

In a future Concentrating Solar Power (CSP) plant, a solar receiver operating with air as a heat-transfer fluid can be used to add high temperature heat in a power plant for continuous and clean power generation. Air is a safe, convenient and cost-free fluid that does not degrade at high temperatures like molten salt. This enables heat addition at higher temperatures for higher power-block thermodynamic efficiencies and a potentially lower cost of power. Refer to [1] for a review of the progress on heat transfer research in CSP.

One proposition making use of a solar air receiver is a Combined Cycle (CC) power plant such as the SUNSPOT power plant concept [2]. Ambient air is compressed to flow into a pressurized air receiver and a downstream combustor to supply hot, high-pressure air to run a gas turbine. The gas turbine generates power during the day and rejects heat to a downstream rock-bed thermal energy storage system which supplies heat to a steam generator and a steam turbine for continuous power generation [3]. A thermodynamic efficiency exceeding 50% may be achieved with a CC CSP plant [4]. Such a plant can be economically competitive in regions with a favourable solar resource such as in the Northern Cape of South Africa [5].

High-pressure air receiver concepts, comprised of metallic or ceramic materials that withstand high temperatures, have been investigated on a pre-commercial scale. Such receivers can be compared on the basis of receiver thermal efficiency: considering reflective, radiative, convective and conductive thermal losses, excluding spillage losses. The SOLUGAS metallic pressurized air receiver has demonstrated the ability to heat air up to 800 °C at a thermal efficiency of around 80% [4]. The advanced Directly Irradiated Annular Pressurized Receiver (DIAPR) air receiver, also known as the Tulip receiver, comprising ceramic components sealed with a glass window has reached and sustained temperatures of 1000 °C [6]. Arguably, durability and scale are limitations for glass windows [7].

* Corresponding author.
E-mail address: erasmusderwalt@gmail.com (D.J. Erasmus).

https://doi.org/10.1016/j.applthermaleng.2023.120529
Received 28 May 2022; Received in revised form 11 February 2023; Accepted 31 March 2023
Available online 14 April 2023

Nomenclature

Variables

α	Absorptivity (–)
d	Diameter (m)
θ	Diffuser half angle (°)
DNI	Direct Normal Irradiance (W/m^2)
η	Efficiency (%)
F	Force (N/m^s)
$\dot{m}$	Mass flow rate (kg/s)
P	Power (W)
p	Pressure (Pa)
$\dot{Q}$	Heat rate (W)
$\dot{q}$	Heat flux (kW/m^2)
r	Radius (mm)
ρ	Density (kg/m^3)
σ	Standard deviation (mrad)
σ	Stress (N/m^2)
T	Temperature (°C)
t	Thickness (mm)
V	Velocity (m/s)
$\dot{V}$	Volumetric flow rate (m^3/s)

Subscripts

abs	Absolute
ap	Aperture
es	Exterior surface
f	Fluid
g	Gauge
h	Hoop
i	Inner
in	Input
nf	Narrow flow
nc	Natural convection
o	Outer
opt	Optical
os	Outer shell
Pyr	Pyromark
rad	Radiative
th	Thermal
t	Total
VM	von Mises

Industrial small scale gas turbines (of around 500 kW) typically operate at around 900 °C and larger axial-flow turbines (of around 150 MW) can operate in the realm of 1300 °C [8]. In either case, a metallic pressurized air receiver can be used to pre-heat air for a downstream combustion chamber or a secondary receiver to reach the required gas turbine inlet temperature.

Low-pressure air has potential to be used as a heat transfer fluid to supply heat at a high temperature with thermal storage for a Rankine cycle plant, a closed-loop supercritical carbon dioxide (sCO_2) Brayton cycle plant or for process-heat applications. An air receiver operating at a low pressure has the advantage of avoiding pressure-related stress.

Low-pressure air receivers have been investigated for a Rankine cycle plant such as in the 200 kW_e pilot plant in Daegu, South Korea by Daesung Energy [9]. This porous media receiver supplies air between 700 °C and 1000 °C to heat a solid thermal storage medium. This circulation loop is then used to generate steam for a steam turbine. A more recent promising exploration of a low-pressure porous-media air receiver estimated by simulation to operate at an air outlet temperature of 1000 °C at a thermal efficiency of around 85% is presented in [10]. Porous-receivers can also exploit quarts glass windows, one such example is [11].

A closed-loop sCO_2 Brayton cycle plant offers a favourable thermodynamic efficiency while thermal energy storage – such as rock bed thermal storage [12] – can be incorporated in the heat transfer loop for dispatchable or continuous power generation if a sufficient heat addition temperature of 650 °C can be reached in the sCO_2 thermodynamic cycle [13].

Metallic air receivers are limited in operating temperature due to material creep and cyclic loading of thermal and pressure stresses at elevated temperatures. Swindeman and Marriott [14] show that, according to the American Society of Mechanical Engineers (ASME) boiler and pressure vessel (BPV) code, the allowable creep stress of high performance nickel and chromium alloys is around 10 MPa at an operating temperature of 950 °C. However, such a limit can be conservative for a solar receiver because such a receiver will also experience creep relaxation (or "stress reset") [15,16]. González-Gómez et al. [15] shows that for a molten salt receiver made of Haynes 230 under a flat aiming strategy operating with a peak crown temperature of between 550 °C and 650 °C, the stress (mostly thermal) at the crown is between 300 MPa and 150 MPa respectively; the lifetime of the receiver is predicted to be around 180 years when accounting for elastic–plastic stress relaxation.

To achieve high receiver outlet temperatures of 800 °C or more while avoiding the stress limits of metallic materials above 1000 °C, a highly effective convective heat transfer device is required. Much effort have been made to enhance the convective heat transfer in receiver absorber tubes, including finned inserts [17,18]. A large convective heat transfer performance can be achieved with an impingement heat transfer device [19]. In such a device, a high velocity turbulent flow impacts onto a surface. A stagnation region is formed at the point of impact, the flow is then redirected by the surface and transitions from laminar to turbulent flow. A thin boundary layer is produced on the impingement surface, enabling favourable heat transfer characteristics.

Various applications of impingement heat transfer in solar receivers have been investigated due to the favourable performance of an impingement heat transfer device. Garbrecht et al. [20] describe a tessellated impinging thermal receiver design that contains hexagon-pyramidal heat transfer devices. Within the components of this device, cold fluid enters through a central pipe, impinges on the inside apex (concave surface) of a pyramid and flows out through finned channels around the pyramidal structure. Craig et al. [21] present an investigation for the implementation of hemispherical dome jet impingement within this receiver. A swirled jet implementation in a central receiver was explored by Quick [22].

Wang et al. [23] and Li [24] present investigations where impinging jets are used within a solar cavity receiver concept. Wang and Laumert [25] present an axial-type impinging jet cavity receiver. Wang and Laumert [25] found that the receiver achieved an outlet temperature of 800 °C, a peak absorber temperature of 1029 °C and a thermal efficiency of 82.8% (without considering convective losses) at an aperture flux of 800 W/m^2.

The Spiky Central Receiver Air Pre-Heater (SCRAP) concept investigated in [26] incorporates protruding spikes to make up a large heat transfer surface area to absorb concentrated solar irradiation. At the high-flux region of each spike, a concave-surface impingement region is employed to absorb thermal energy. To improve the heat transfer and pressure loss characteristics of the impingement region in the SCRAP concept from a conventional impinging jet, the Tadpole heat transfer enhancement device was conceived [27].

The Tadpole incorporates impingement heat transfer with pressure recovery. The flow domain of the Tadpole is depicted in Fig. 1. In the Tadpole's domain, the inlet flow is accelerated in a nozzle to impinge

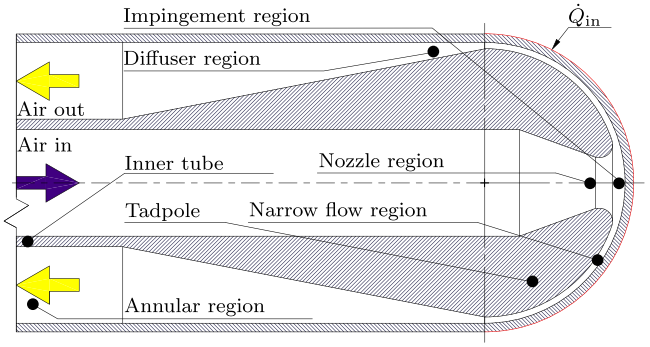

Fig. 1. Illustration of the Tadpole's flow domain.

within a concave surface. The flow is then confined to a narrow flow region at an elevated velocity to maintain a thin boundary layer for favourable heat transfer performance [27]. The flow is then expanded in a diffuser to recover the previously developed dynamic pressure for favourable pressure loss characteristics.

The Tadpole has many geometric degrees of freedom that can be exploited to obtain a favourable combination of heat transfer and pressure loss characteristics. It has been demonstrated experimentally that the Tadpole can improve the heat transfer and pressure loss performance characteristics in comparison with a conventional impinging jet [27]. The Four-Equation Transition SST turbulence CFD model has been validated for use in the Tadpole's domain [27].

Instead of employing the Tadpole as a heat transfer enhancement such as in the SCRAP concept [28], a new concept – a tessellated-impinging receiver – was conceived with the idea of maximizing the usage of the Tadpole concept due to its favourable heat transfer performance relative to a conventional impinging jet. The use of the Tadpole as the basis of heat transfer in a solar receiver is novel. The concept is presented in Fig. 2. It contains multiple Tadpole units within hemispherical domes in a tessellated layout — similar to a honeycomb; with each unit having a hexagonal base. Favourable thermal absorption performance is expected due to the elevated impingement heat transfer coefficient within the Tadpoles. The receiver is similar to the one presented in [20] in that it makes use of impingement and hexagonal tessellation.

The base region of a hemispherical unit is substantially protected from reflective and radiative heat losses due to the base region being nearly perpendicular to the aperture. The receiver also may contain a secondary reflector to recover (by re-reflection) spillage — incoming solar irradiation that does not directly reach the heat transfer units. The secondary reflector is also expected to reduce convective heat losses.

The objectives of this paper are to develop a thermal model of the tessellated-impinging receiver and to investigate the thermal performance characteristics of the concept for application as a high- and low-pressure air receiver. The secondary reflector will not form part of the scope of this initial outlook, neither will thermal stresses, nor the quantification of reflective losses and convective losses; instead, assumptions will be made for these losses.

1.2. Layout of paper

In Section 2, significant design considerations including the mechanical stress, dimensional scaling and fluid dynamics are first explored, a reference design is then chosen. In Section 3, a heliostat field and a suitable aiming strategy are subsequently developed to model the incoming concentrated irradiation. The resulting incoming flux distribution for a single characteristic receiver unit is then extracted. Section 4 describes a Computational Fluid Dynamics (CFD) investigation of this unit to finally arrive at an initial performance outlook of the concept at various operating conditions in Section 5.

2. Reference design development

2.1. Mechanical stress considerations

A pressurized air receiver resists the gauge pressure of its heat transfer fluid at an elevated operating temperature where creep is pertinent. It also experiences stresses from thermal gradients. The effect of thermal stresses on absorber tubes have been investigated by Pérez-Álvarez et al. [29]. Thermal stresses for a receiver operating at over 800 °C are significant but will be neglected in this investigation. Although pressure-related stress will be considered.

Inconel 718 was chosen for this application because the thermal properties are well described in literature and demonstrates favourable creep strength characteristics. The pertinent mechanical stress here is the stress occurring within the hemispherical dome. Dowling [30] presents thick-walled pressure vessel equations for a hemisphere. Eq. (1) gives the axial (σ_x) and hoop stress (σ_h) as a function of the radius, r:

$$\sigma_{x\ (r)} = \sigma_{h\ (r)} = \frac{p_g r_i^3}{r_o^3 - r_i^3}\left(\frac{r_o^3}{2r^3} + 1\right), \tag{1}$$

where r_i is the inner radius of the hemisphere and r_o is the outer radius. Similarly, Eq. (2) gives the radial stress, $\sigma_{r\ (r)}$:

$$\sigma_{r\ (r)} = -\frac{p_g r_i^3}{r_o^3 - r_i^3}\left(\frac{r_o^3}{r^3} - 1\right). \tag{2}$$

Additionally, the dome region tensile stress caused by: firstly, the thrust generated in the Tadpole's nozzle region impacting onto the hemisphere and secondly, the outlet thrust of the Tadpole's narrow flow region (depicted in Fig. 1) can be accounted for through a linear momentum balance: $F_x = \dot{m}_{unit}(V_n + V_{nf,out})$, where V_n is the nozzle's outlet velocity and $V_{nf,out}$ is the narrow flow region's outlet velocity. This contribution to the overall stress is relatively small in comparison to that of the gauge pressure (for a high-pressure operating condition). Nevertheless, the force must be withstood by the dome and transferred through its base in the axial direction. The stress contribution over the base area ($\sigma_{x,F}$) is given in Eq. (3):

$$\sigma_{x,F} = \frac{F_x}{\pi(r_o^2 - r_i^2)} \tag{3}$$

It was found that the peak stress characteristically occurs on the inside of the hemisphere at the base in tension.

2.2. Dimensional scaling sensitivity

Considering the complexity of investigating and manufacturing a receiver based on hundreds of repeating units as shown in [20,31], a solution may be to limit the number of repeating units in the receiver by maximizing the size of individual units.

To understand the effect of increasing the outer-shell thickness (t_{os}), an example of Fourier's law of (1D) thermal conduction in spherical coordinates follows. Using an Inconel thermal conductivity of 25 $\frac{W}{mK}$[1] and an absorbed heat flux of 500 $\frac{kW}{m^2}$: the temperature drop over the outer shell follows $\frac{\Delta T}{t_{os}} \approx 20.03\ \frac{°C}{mm}$.[2] It is therefore important to maintain a minimal outer-shell thickness to reduce thermal losses caused by the temperature gradient through it.

An up-scaling sensitivity is now demonstrated for a constant operating gauge pressure and a constant outer-wall thickness to observe the peak von Mises stress with an increasing unit hemispherical radius, r_o. The peak von Mises stress increases by ×3.67 for a ×4 increase in

[1] For Inconel 718 at around 870 °C [32].

[2] This calculation was conducted with an exterior curvature radius of 35 mm and differs from the flat plate calculation by 0.1%.

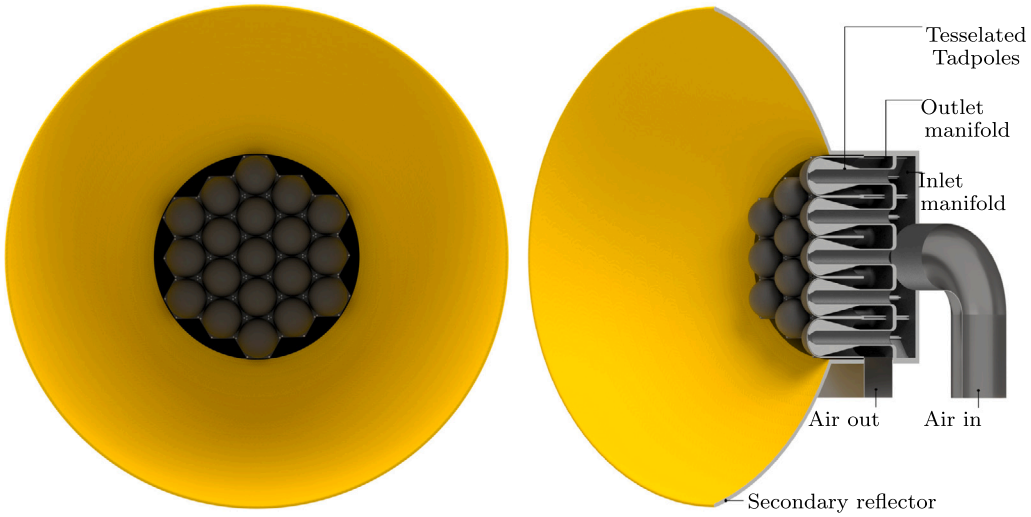

Fig. 2. The tessellated-impinging central receiver concept.

dimensional scale. Therefore, to withstand increased pressure stress, it will be required to up-scale t_{os} along with r_o to avoid high stresses.

It is demonstrated that up-scaling receiver units creates the concern of an increased gauge pressure stress with a thin wall thickness for a pressurized air receiver. Whereas for a low-pressure air receiver, dimensional scaling is a less significant issue. The effect of the dimensional scaling of a unit on the heat transfer performance will be explored later in Section 5.

Alternatively to up-scaling an individual unit, the number of receiver units along with the aperture size can be increased or decreased to scale the receiver for a desired thermal requirement if a substantially uniform aperture flux distribution can be achieved — although this does not achieve the goal of reducing manufacturing complexity.

2.3. Input solar flux magnitude

A larger input flux density, $\dot{q}_{in}$, results in a larger thermal output for a relatively small receiver size. Along with a smaller surface area, the area from which thermal losses occur is also less. In support of this observation, it has been modelled that the CentRec particle receiver has seen a thermal efficiency benefit with increased flux concentration from 200 kW/m^2 to 1000 kW/m^2 [33]. However, because the metallic receiver of the present study requires thermal flux to move through its outer shell, the proportional temperature drop over the shell thickness is significantly larger with an increased flux concentration. This creates a potential trade-off of an appropriate concentration. Accordingly, both a peak concentration of 2500 kW/m^2 as well as half of this will be explored in this study to identify whether a significant sensitivity occurs due to flux concentration.

The previously outlined experimental air receivers were demonstrated at a thermal output power range between 0.4 MW_{th} to 3.2 MW_{th}. The initial outlook on the receiver will therefore target a thermal output of 1 MW_{th} — a heliostat field will be developed around this target and an aperture diameter of 1 m is chosen for the tessellated structure. The 1 m aperture is chosen as a starting point to enable a thermal investigation, not as a recommendation of a final size, the tessellated units can be scaled to an arbitrarily large aperture size.

2.4. Reference domain

The reference domain model is isolated to only the heat transfer region of the concept. The inlet, the manifolds and the outlet of the receiver are thus excluded from the simplified model. These components increase the overall pressure losses. The maximum dynamic pressure experienced in the heat transfer region of a receiver unit is around 6 orders of magnitude greater than that experienced in the excluded components. Total pressure losses are directly proportional to the dynamic pressure [34]. This indicates that the excluded components represent negligible pressure losses.

The Tadpole's performance as a heat transfer device is detailed in [27]. The reference manifestation investigated here was guided by the previous heat transfer investigation; this manifestation was formed iteratively with the objective of obtaining a large heat transfer coefficient at an acceptable pressure loss.

In general, it is desirable to constrain the Tadpole's domain to develop a similar flow area at its inlet and outlet to develop similar dynamic pressures in these regions. This can avoid unnecessary expansion losses because the required area ratio over the diffuser is not unnecessarily large. The diffuser's expansion half angle is conservatively small ($\theta_h = 6.5°$) because the suitability of a conservatively small diffuser half angle was observed in [34].

Fig. 3 gives the reference dimensions for a 30° sector of a receiver unit: this is the simplest representation to capture the geometry of the hexagonal tessellation structure in a unit. A spline describes the bulbous portion of the Tadpole with the aim to develop a relatively constant velocity within the narrow flow region. In Fig. 3, the spline is constrained using three thickness dimensions through the progression of the narrow flow region. It is shown that the thickness reduces near the middle of the narrow flow region in order to substantially maintain the peak Mach number developed at the start of the narrow flow region. It is depicted that the thickness of the narrow flow region (0.768 mm) is small and will be sensitive to thermal and pressure deformation. This is a limitation in the design and can be improved by up-scaling for a low-pressure application. The chosen outer shell wall thickness of 2 mm was chosen in order to keep the Von-Mises stress below 10 MPa — the creep rupture strength of this material at 800 °C. As previously discussed, creep relaxation also occurs in such applications, although this has not been modelled here. Therefore a conservative mechanical stress limit was chosen.

Fig. 4 depicts a top-down overview of the process to estimate the thermal efficiency of the SUNflower. The various parts of this model will be described in the proceeding two sections.

3. Heliostat field integration

3.1. Introduction

For a more holistic understanding of receiver's operational performance, the exploration now expands to include the heliostat field.

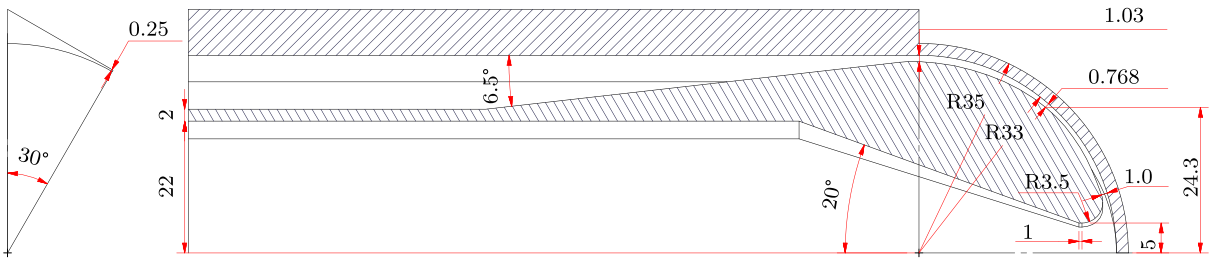

Fig. 3. Dimensions (in mm) of a 30° sector of a receiver unit.

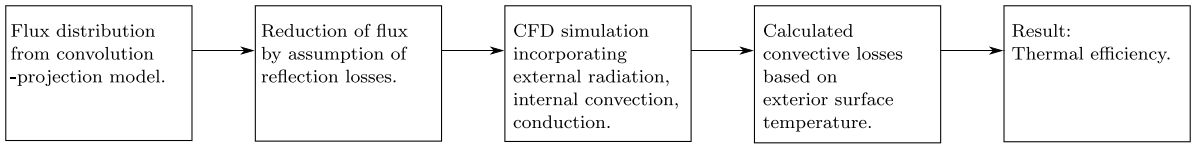

Fig. 4. Flowchart describing the process to estimate thermal efficiency.

The incoming solar flux distribution of a receiver can be largely uniform or non-uniform. The set of aiming points of the heliostats on the receiver, controlled by the aiming strategy, affects the receiver's flux distribution. Single point aiming causes a high peak flux magnitude on a receiver aperture with a weak flux gradient in the radial direction around its peak. A multi-point aiming strategy producing a uniform flux profile affects a more homogeneous receiver surface temperature distribution and reduced thermal stresses compared with a single aiming strategy [35]. However, the consequential high flux density imposed near the edges of the aperture causes increased spillage losses when compared with single aiming.

If single aiming is implemented on the receiver, it would be necessary to model multiple repeating units to incorporate effects such as net radiative heat transfer between the exteriors of units as well as the mixing of air flows from units with varying outlet temperatures — this kind of analysis was done by Craig et al. [19].

However, if an aiming strategy is employed to produce a uniform flux on the receiver so that the flux absorbed by neighbouring units is similar then the radiation interaction between neighbouring units would be symmetric along the tessellated symmetry boundaries. And the variation of outlet temperatures between receiver units would be negligible. This firstly enables the receiver to achieve higher surface and outlet operating temperatures because the overall surface temperature distribution can be constrained nearer to the material's allowable limit without first reaching failure at the peak flux region of the aperture. Secondly it enables a simplified analysis of the receiver's performance because only a single repeating unit needs to be considered. The objective is thus to incorporate a heliostat field with such an aiming strategy to produce a relatively uniform flux distribution on the receiver.

3.2. Flux modelling

To develop the aiming strategy, the flux distribution from the heliostat field on a central receiver aperture must be modelled. This can be done using the Monte-Carlo Ray-Tracing (MCRT) approach or using a convolution-projection method.

Cheng et al. [36] investigate a pressurized volumetric receiver by integrating MCRT modelling with a finite volume method (FVM) thermal model. Slootweg et al. [37] investigate a molten salt receiver using CFD with the integration of MCRT. However, MCRT is highly computationally expensive.

Sánchez-González et al. [38] explores the use of a convolution-projection method that requires two orders of magnitude less computational time than MCRT.[3] For this reason, the convolution-projection method will be implemented in this work. A convolution-projection method consists of two operations. Firstly, the flux distribution produced by each heliostat on the image plane (receiver aperture) is determined by means of a Gaussian function resulting from the mathematical convolution of the solar intensity distribution from the sun (sun shape) and mirror surface slope error (σ_{slope}). Secondly, the resulting image plane flux distribution is projected onto the discretized receiver surface.

The code from [38] was validated with experimental data from the Plataforma Solar de Almería and the SolTrace MCRT software. This convolution model is used to model the flux distribution on the receiver. The convolution model considers the following characteristic losses incurred by a heliostat field: spillage, blocking, shading, cosine, reflectivity and attenuation.

3.3. Heliostat field

It was found that a field containing small heliostats is better suited for a uniform flux aiming strategy because small heliostats produce small beam images on the aperture and so less spillage would be observed on the aperture compared to large heliostats. The Heliopod [39] was accordingly chosen. The heliostat modelling parameters required to reproduce the results are given in Table 1. The refined field layout parameters are given in Table 2. The tower height was optimized to reach a maximum single aiming overall field efficiency at equinox noon. The SUNflower's tilt angle was chosen to approximate that of the previously discussed Tulip receiver [6]. The tower height was optimized to reach a maximum single aiming overall field efficiency at equinox noon.

A relatively uniform aperture flux distribution is particularly desirable for this receiver concept. A 1 m (diameter) discretized 2D circular aperture was used in the development of a new aiming strategy implementation. The implementation is called Blossaim and is applicable for circular apertures and polar heliostat fields [42].

The resulting Blossaim aperture flux concentration map is compared with a single aiming strategy (where all heliostats aim at the aperture's

[3] The program can be downloaded from https://ise.uc3~m.es/research/solar-energy/fluxspt/.

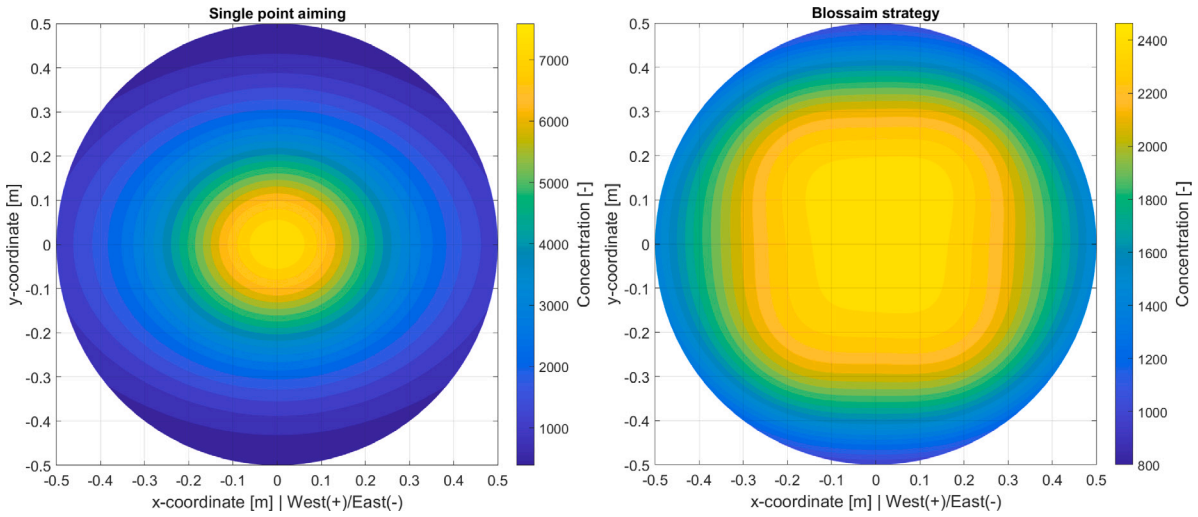

Fig. 5. Comparison of flux distributions between single point aiming (left) and the Blossaim strategy (right) at 12 pm solar time during equinox. *Source:* Adapted from [42].

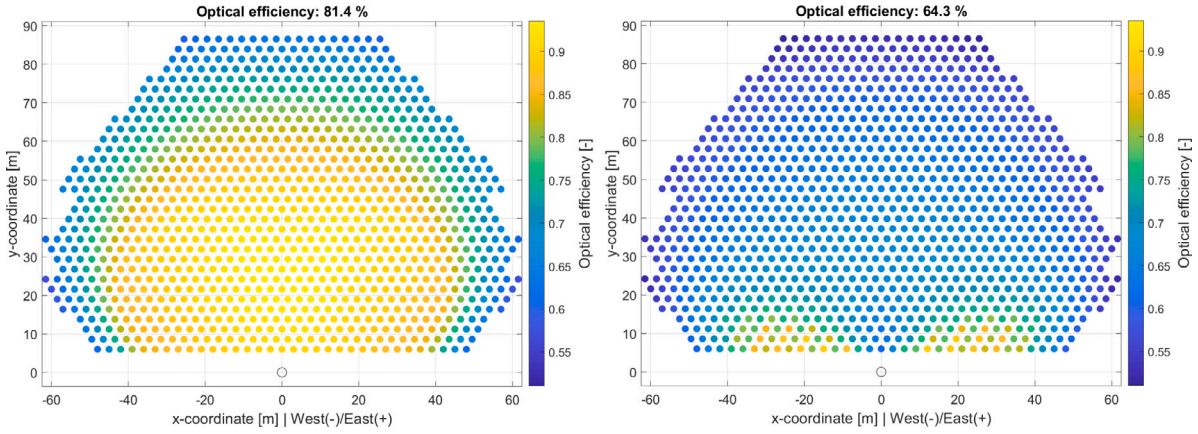

Fig. 6. Optical efficiency distribution of the heliostat field for single point aiming (left) and the Blossaim strategy (right) accounting for the losses described in Section 3.

Table 1
Modelling parameters of the heliostat field.

Parameter	Unit	Assumption
Mirror reflectivity	[%]	95
Sun shape	[–]	Circular Gaussian
Sun shape standard deviation	[mrad]	2.09,[a]
Surface slope error standard deviation (σ_{slope})	[mrad]	1.2,[b]
Geographic latitude (PS 10, Seville)	[°]	37.442 26
Solar direct normal irradiance (DNI)	$[\frac{W}{m^2}]$	1000

[a] [40].
[b] [41].

Table 2
Layout dimensions of the heliostat field and receiver.

Parameter	Unit	Dimension
Heliostat		
Width	[m]	1.83,[a]
Height	[m]	1.22,[a]
Height from ground to reflective mid-point	[m]	1.5,[a]
Heliopod triangular boundary length	[m]	6.0,[a]
First row displacement	[m]	6.0,[b]
Count	[–]	1068
Receiver		
Aperture diameter	[m]	1.0,[b]
Tilt	[°]	32.5,[b]
Height	[m]	36,[c]

[a] [39].
[b] Design decision.
[c] Optimized for the given tilt angle.

centre) in Fig. 5. The dimensionless flux concentration depicts the ratio of incident flux and DNI. The corresponding map of heliostat optical efficiency is shown in Fig. 6. The Blossaim strategy achieves a relatively uniform flux distribution on the aperture with a 66% reduction in the peak flux. The deterministically arranged aiming points produce a flux distribution that is robust to a changing field optical efficiency distribution with solar time [42].

Table 3 shows the overall optical efficiency of Blossaim is 17.1% lower than the single aiming strategy because of increased spillage losses from all heliostats aimed near the edge of the 1 m aperture. The

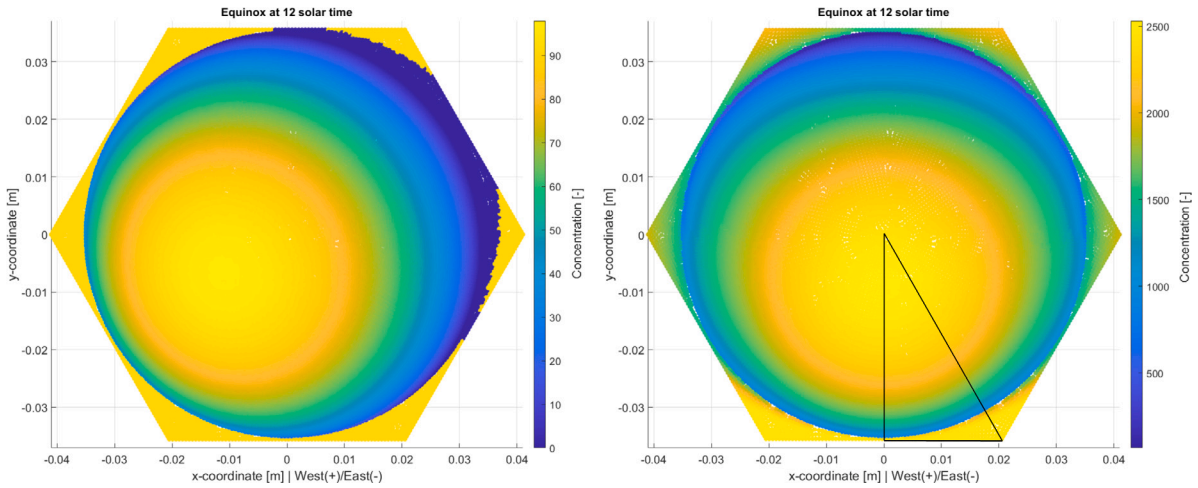

Fig. 7. Relative flux image from a single heliostat (left) and from the entire field (right) on a central receiver unit with the selected region showing the reference heat source boundary condition to be interpolated into the CFD model; for a sense of scale the exterior hemispherical diameter is 70 mm.

Table 3
Comparison of field optical efficiency between a single aiming strategy and the Blossaim strategy for a 1 m aperture and an extended aperture with the previous aiming points.
Source: Adapted from [42].

Aperture diameter	Single aiming	Blossaim
1.0 m	81.4%	64.3%
1.5 m	88.6%	86.6%

spillage losses incurred can be reduced significantly by extending the acceptance aperture for the same aiming points as before. By opening up the aperture by 50% to 1.5 m, the optical efficiency reduction with Blossaim becomes only 2%. The idea is that a secondary reflector should be used to extend around the 1 m aperture to 1.5 m or larger, capturing the spillage and directing it towards the flux gradient region near the aperture edge, although this has not been investigated in this scope.

3.4. Applying the convolution flux projection to the receiver's surface

On the absorber surface, the hemispherical domes slightly shade incoming flux (from some heliostats) from reaching deeper regions of the receiver's exterior. The convolution-projection model accounts for this with a calculation on each discretized surface node which determines whether the node is blocked by another node. These effects are demonstrated in a relative flux distribution from a single heliostat on an isolated central receiver unit (shown on the left) in Fig. 7. The overall flux distribution is obtained from the superposition of the flux images from all the heliostats (shown on the right of the figure). Computational reflection modelling has been excluded from this exploration, it will be accounted for as an assumption. However, re-radiation will be considered in the following section.

The next step is to explore the unit's thermal performance using CFD by applying this flux distribution as the heat source, this will be referred to as the 'HF' (high-flux) configuration. This distribution will also be scaled so that the heat transfer performance can be explored over a range of area-weighted-average flux magnitudes: namely to explore a low flux (LF), a very low flux (VLF) and an up-scaled (US) version which will be depicted in the results section.

4. CFD modelling

4.1. Overview

The CFD flow domain is similar to the ANSYS Fluent® model described in [27] where the Four-Equation Transition-SST turbulence

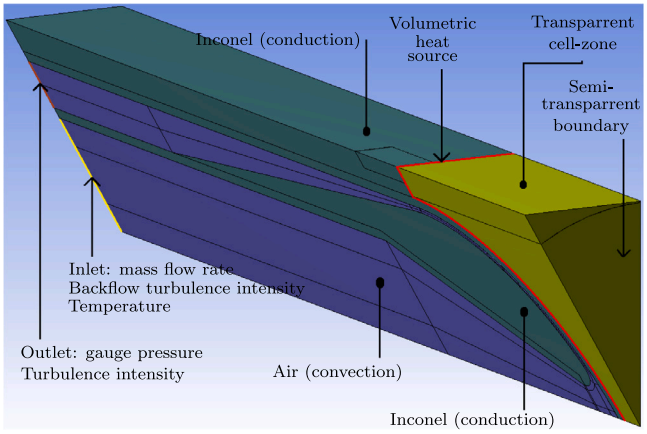

Fig. 8. Flow domain of the CFD model.

model was validated for the Tadpole's domain. The difference is that this model has a 3D domain with symmetry boundary conditions on the sides of the sector. Fig. 8 describes the flow domain of the 3D CFD model. Conduction and convection outside of this domain are neglected.

Three faces are depicted in Fig. 8: the transparent boundary as well as two of the three symmetry boundaries. The sector makes up the 1/12 repeating part of an axial revolution. The inlet and outlet boundary conditions are shown in the figure along with the assigned cell-zones. Heat originates from the volumetric heat source primarily towards the convection domain through the outer shell but also in the opposite direction — through the transparent cell-zone and the semi-transparent boundary through radiation as a thermal loss to ambient. The exterior surface in the reference design is coated with Pyromark 2500 paint. The emissivity and absorptivity are modelled. Concerning internal radiation modelling (between the Tadpole and the interior heat transfer surface), the emissivity of Inconel is applied.

Variable thermal conductivity in terms of temperature was modelled using data from [32]. For the air properties, correlations also based on [43] for μ, c_p and k were used. The assumed constant thermal properties can be found in Table 4.

It is required to apply the receiver's surface flux distribution from the convolution-projection model to the CFD model. The procedure presented in [46,47] for the implementation of a volumetric heat source in ANSYS Fluent® is adopted here. Heat generation rate with a thin

Table 4
Material properties.

Material	ε [–]	α [–]
Inconel 718 (648 °C)	0.841,[a]	0.841,[c]
Pyromark 2500 (967 °C)	0.9,[b]	0.95,[b]

[a] [44].
[b] [45].
[c] Kirchhoff's law of thermal radiation was assumed.

cell-zone is required instead of heat flux on a surface to enable flux to be absorbed through the receiver and also radiated outwards from it. The receivers exterior surface is modelled as a 3D volume (volumetric heat source in Fig. 8) with an assigned arbitrary thickness – in this case 0.01 mm – to create a thin cell zone. A 3D heat flux distribution (shown in Fig. 7) is converted to a 3D heat generation rate distribution (from W/m^2 to W/m^3) by dividing the flux at each cell with the thickness of the thin volume (0.01 mm). The heat source profile is transported in a text file that contains a list of 3D surface coordinates along with the heat generation rate. Fluent® interpolates this heat generation rate distribution into the cell zone (as depicted in Fig. 8).

The incoming flux modelling approach does not account for reflection from the receiver surface because the input boundary condition is a volumetric heat source on the surface, not a radiation boundary condition. Therefore, an assumption must be made to model the reflective losses. The reflective losses from the incident aperture radiation can be approximated conservatively by assuming a relative loss of $1-\alpha_{Pyr}$, the complement of the absorptivity of the Pyromark surface coating. This sets the upper limit of this loss to 5%. This limit would apply for a flat plate absorber surface. However, the absorber substantially traps reflective losses because parts of its surface does not directly face ambient. Garbrecht et al. [20] reported reflective losses of 1.3% from their similar pyramidal receiver using the same absorptivity constant. The reflective losses are hence assumed as an average of these values: 3.15%.

This leaves the radiative heat losses to be modelled. The exterior of the receiver's surface interacts with the sky and the ground through radiation. This is modelled with the Discrete Ordinates (DO) radiation model. The DO model performs the solution of the Radiative Transfer Equation for each computational cell on a 3D quadrant of space and considers two solid angles, subdivided into discrete ordinates with additional pixelation applied as described above. All directions of radiation are therefore considered, with the spectral range or wave number dependent on the local temperature of nearby surfaces. This implies that the DO method is calculating thermal re-radiation between all participating surfaces in response to the solar irradiation heat source obtained through convolution as described in Section 3. The DO discretization resolution — the divisions and pixels per degree of the angular space were increased from the default Fluent® values to a value of 3 due to large temperature gradients in the interacting surfaces.

A semi-transparent wall boundary with a fixed boundary condition external radiation temperature of 25 °C (and an emissivity and diffuse fraction of 1) is modelled at a small distance away from the exterior surface to represent the aperture. Between the aperture and the receiver's surface is a cell-zone through-which radiation can freely travel (as depicted in Fig. 8). This zone has negligible thermal conductivity and is modelled as a transparent solid. Heat transfer by natural convection through the exterior air is therefore not modelled computationally. The radiative heat transfer between receiver units is considered to occur symmetrically – the neighbouring units are assumed to operate at the same temperature distribution. The symmetry boundaries previously shown in Fig. 8 act like mirrors using the DO model to emulate the neighbouring units (within the tessellated structure) around the simplified symmetric domain. Radiative heat transfer between the inner walls of the heat transfer unit is also modelled using the DO model.

For the initial outlook, only a rough estimation of convective losses is sought. Natural and forced convection thermal losses have been explored in [48]. For an open cavity receiver, a natural convection heat transfer coefficient has been correlated:

$$h_{nc} = 0.81(\overline{T_{es}} - T_{\infty})^{0.426}, \tag{4}$$

where the heat transfer coefficient is applicable to the entire internal surface of the cavity — hence the area applied must account for the absorber and any additional internal surfaces. For this initial estimation of natural convective losses ($\dot{Q}_{nc}$), it is assumed that the total internal cavity area is 2× the exterior absorber area and operates at the same temperature. This area assumption is made because the design of the secondary reflector is not the focus of this work. An ambient temperature of $T_{\infty} = 25$ °C is assumed.

The thermal efficiency (η_{th}) is now derived in terms of the ratio of the absorbed heat rate by the fluid ($\dot{Q}_f$) and the incoming heat from the heliostat field excluding spillage ($\dot{Q}_{in}$):

$$\eta_{th} = \frac{\dot{Q}_f}{\dot{Q}_{in}}. \tag{5}$$

The next step is an energy balance on the receiver:

$$\dot{Q}_{in} = \dot{Q}_f + \dot{Q}_{rad} + \dot{Q}_{refl} + \dot{Q}_{nc}, \tag{6}$$

where $\dot{Q}_{rad}$ is radiative losses (excluding reflective losses), $\dot{Q}_{refl}$ is reflective losses (assumed 3.15% of $\dot{Q}_{in}$ as detailed earlier in Section 4.1[4]), $\dot{Q}_{nc}$ is natural convective losses. After making the reflection loss assumption, the equation is then equivalent to:

$$\dot{Q}_{in} = \dot{Q}_f + \dot{Q}_{rad} + \dot{Q}_{nc} + 0.0315\dot{Q}_{in}, \tag{7}$$

substitution of the energy balance into the efficiency ratio yields our efficiency equation:

$$\eta_{th} = (1 - 0.0315)\frac{\dot{Q}_f}{\dot{Q}_f + \dot{Q}_{rad} + \dot{Q}_{nc}}. \tag{8}$$

4.2. Computational considerations

The Coupled pressure–velocity scheme was used. For spatial discretization: Green–Gauss cell-based was used for the gradients; second-order was used for pressure; second-order Upwind was used for the energy equation, density, momentum, turbulence kinetic energy and turbulence dissipation rate; finally, the first-order Upwind scheme was used for intermittency and the Discrete Ordinates model.

The computational mesh is shown in Fig. 9. The internal convection domain is fully structured and revolved about the axis, whereas the conduction domains and the transparent cell-zones are unstructured. The structured convection domain enables obtaining sufficient grid resolution near the wall for the turbulence model at a reasonable cell count to run overnight on a cluster. To assess grid independence, a coarse mesh and a fine mesh containing 1.3×10^6 elements and 6.6×10^6 elements respectively were investigated with the fine mesh resembling about double the cell divisions of the coarse mesh.

After 6000 iterations, the air flow temperature change and the total pressure loss varies between the coarse and fine mesh by 0.910% and 1.53% respectively. The peak y^+ value in the fine mesh convection domain was around 0.88 which is sufficient for this turbulence model. Stable convergence on the outlet temperature and pressure loss was confirmed. This assures confidence on the results of the fine mesh to be used for further calculations.

[4] As detailed earlier in this section, the heat input boundary condition does not enable modelling reflected radiation. Therefore the reflective loss is artificially incorporated.

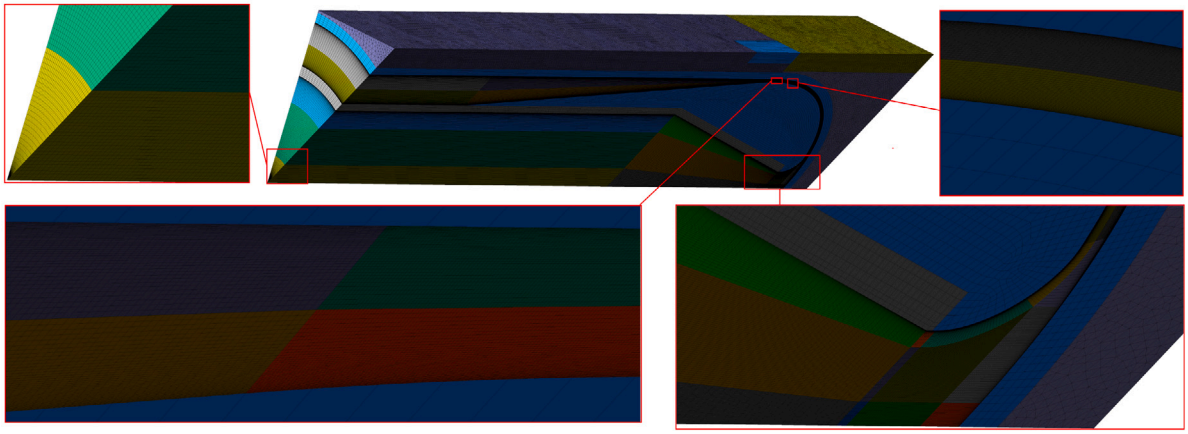

Fig. 9. Computational mesh of the flow domain.

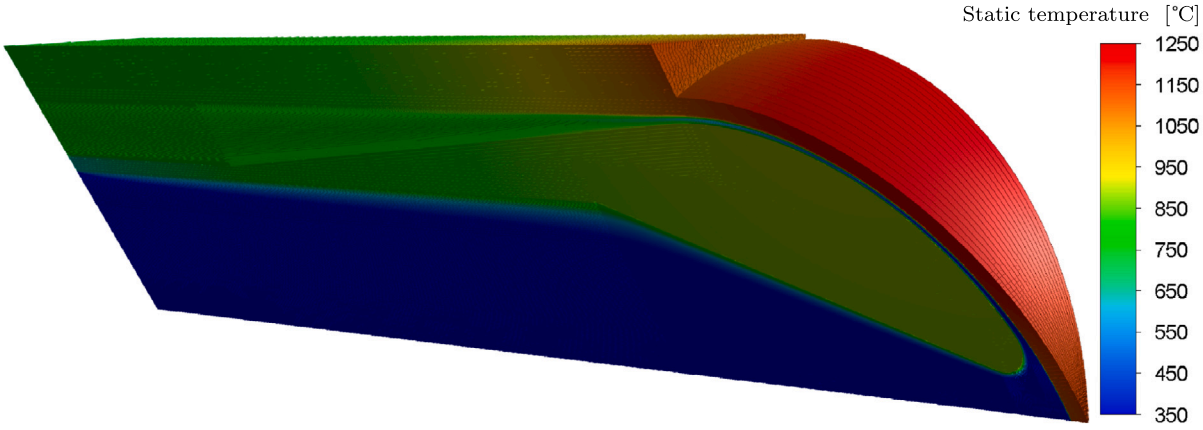

Fig. 10. Temperature contour of the (high-pressure, very-low-flux) receiver unit showing the required exterior Inconel temperature to heat the air flow to 800 °C.

4.3. Uncertainty in the CFD domain

An uncertainty assessment follows of the calculated efficiency, due to the symmetry boundary conditions in the simplified 3D domain shown in Fig. 8. The symmetry boundary (characteristically receiving the highest re-radiative flux of the three symmetry boundaries) was replaced with the physical reflection of the outer shell with the temperature profile of the original surface while the exterior air domain and aperture boundary was extended over the reflected domain. The reflected temperature profile was iterated until its average temperature corresponded within 4 K of the original surface. This resulted in a 0.33% reduction in efficiency and a 127 K (7.68%) increase in average surface temperature. The reflection test case demonstrates that the symmetry boundary marginally affects the efficiency whilst creating a substantial uncertainty in the temperature of the outer shell. This test case represents the expected uncertainty of the proceeding results.

5. Results

The concept's capability of heating an air flow from 351 °C to approximately 800 °C was investigated at varying operating irradiation and pressure conditions. Fig. 10 illustrates the heating of the air flow for the most favourable (high-pressure, very-low-flux) operating condition. The figure shows a peak in surface temperature at around midway through the narrow flow region.

The temperature of the Tadpole's volume is higher than the flow temperature as it is being significantly heated by internal radiation. A developing thermal boundary layer is accordingly observed on both surfaces of the narrow flow region and the surface of the inner tube

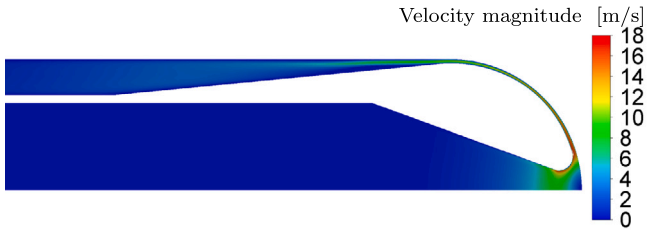

Fig. 11. Velocity-magnitude contours of the (high-pressure, very-low-flux) receiver unit.

and nozzle. Fig. 11 depicts the velocity magnitude distribution through the domain, the flow is accelerated by the nozzle and maintained at an elevated velocity in the narrow flow region to create a thin boundary layer for an elevated heat transfer coefficient [27]; thereafter the flow is decelerated in the diffuser for pressure recovery. The set of operating and performance characteristics of a receiver unit is shown in Table 5. This set of cases was iteratively produced to explore the performance characteristics.

The thermal efficiencies achieved for all cases were relatively low when compared with what has been estimated by prior literature for pressurized receivers. This is attributed to the high exterior surface temperature ($\overline{T_{es}}$) causing the dominating heat losses to be radiative heat losses (the fourth power of Stefan–Boltzmann law explains it) (up to 40%), with natural convective losses estimated below 5%. The thermal efficiency improves by reducing the flux from 2530 kW/m^2 to 1270 kW/m^2. At lower fluxes, lower surface temperatures are observed

Table 5
Operating characteristics of the receiver unit cases: where 'H', 'L' and 'VL' indicate high and low and very low; 'P' and 'F' indicate pressure and flux, 'IM' represents an increased mass flow rate and 'US' represents an up-scaling of ×4 in dimensions with the same outer-shell thickness.

Parameter	Unit	HP, HF	LP, HF	HP, LF	HP, VLF	LP, LF	HP, LF, IM	LP, LF, US
Boundary conditions								
$\dot{m}_{\text{unit}}$	$[\frac{\text{kg}}{\text{s}}]$	0.016 97	0.016 97	0.008 904	0.004 500	0.008 904	0.0228	0.1030
$\dot{q}_{\text{in,max}}$	$[\frac{\text{kW}}{\text{m}^2}]$	2530	2530	1270	635	1270	1270	1270
T_{in}	[°C]	351	351	351	351	351	351	351
$p_{\text{out,abs}}$	[kPa]	1007.9	202.65	1007.9	1007.9	202.65	1007.9	202.65
Results								
T_{out}	[°C]	801.1	800.2	800.4	801.2	799.3	565.2	799.7
$\overline{T_{\text{es}}}$,[a]	[°C]	1691	1690	1383	1142	1383	1166	1498
η_{th}	[%]	57.3	57.2	59.3	59.3	59.2	69.9	46.2
Δp_{t}	[kPa]	4.78	28.0	1.64	0.564	8.49	6.06	2.94
$\dot{Q}_{\text{f}}$	[kW_{th}]	8.44	8.43	4.45	2.28	4.44	5.18	51.7
$P_{\text{loss,fluid}}$	[W]	18.2	489	3.29	0.572	82.4	28.1	335
$\sigma_{\text{VM,peak}}$,[b]	[MPa]	8.41	0.952	8.40	8.40	0.943	8.41	3.45

[a] Average hemisphere exterior temperature.
[b] Peak mechanical von Mises stress.

and thereby lower radiative losses; but not when reduced further to 635 kW/m^2 (where the share of convective losses increases). Even for the most favourable very-low-flux case, the surface temperature exceeds 1000 °C. Eq. (9) depicts the convection heat transfer equation,

$$\dot{Q}_{\text{conv}} = hA(T_{\text{s}} - T_{\text{f}}). \tag{9}$$

Accordingly, in a thermal receiver employing convective heat transfer, a large thermal absorption ($\dot{Q}_{\text{conv}}$) is desired along with a small temperature difference between the heat transfer surface and the fluid ($T_{\text{s}} - T_{\text{f}}$) in order to avoid overheating of the material. To achieve this, a large product of the heat transfer coefficient and the surface area (hA) is required.

The lesson from these findings is that, although the convective heat transfer performance of the Tadpole is relatively high, the receiver does not exhibit a large surface area. The ratio of: the exterior surface area and the aperture area ($A_{\text{es}}/A_{\text{ap}}$) of the receiver concept is insufficient for this high flux and high outlet temperature in limiting the metal temperature to acceptable levels. For the SUNflower, this ratio is 2, it is estimated that the SOLUGAS concept has a ratio of around 9 and the SCRAP concept has a ratio of 5. The SUNflower has a relatively small surface area ratio, the unfavourable thermal efficiency is attributed to this small surface area ratio. The small surface area ratio leads to a large radiative view factor to ambient for losses to occur. Because of the small surface area, the air flow rate must be small to obtain the $\Delta T \approx 450$ °C to reach $T_{\text{out}} \approx 800$ °C causing a relatively low internal heat transfer coefficient compared to what the device can achieve at higher flow rates. For this concept, the small exterior surface area is therefore a limitation in the design. Further iteration of the design and boundary conditions can be performed to achieve the surface temperatures below 1000 °C. The exterior temperature may be reduced by applying an incident flux below the presently considered 635 kW/m^2. The surface-area-to-aperture ratio can be increased to improve the thermal efficiency.

In Table 5, the high-pressure, low-flux (HP, LF) case can be compared with the SCRAP concept as modelled in [26] because both cases operate under a similar incident flux (1270 kW/m^2) and outlet temperature (800 °C). The SCRAP concept has been predicted to perform at a significantly higher thermal efficiency and a lower exterior surface temperature. Both the SCRAP and the SOLUGAS concepts make use of significantly larger exterior surface areas ($A_{\text{es}}/A_{\text{ap}}$) and achieve 800 °C at higher thermal efficiencies.

To observe if the surface temperature can be improved, a higher mass flow rate case is explored (HP, LF, IM). Here, the mass flow rate is increased from the HP, LF case until the outlet temperature is in the vicinity of that of a molten salt receiver — since below this temperature, air as a heat transfer fluid does not pose an advantage over molten salt's degradation temperature. Table 5 depicts that the surface temperature and thermal efficiency significantly improves, although it is still above 1000 °C.

Table 5 shows that the high-pressure test cases undergo significantly lower pressure losses than the lower pressure cases. For example, the HP, HF case shows a 82.9% reduction in Δp_{t} from the LP, HF case. This suggests lower pumping losses for a high-pressure receiver. Although pressure losses are not the only variable affecting the pumping losses, it was hence sought to estimate the fluid pumping power loss. The power dissipation through a reduction in total pressure can be estimated using the Bernoulli equation from [49]; with the simplifying assumptions of 1D adiabatic incompressible flow: $P_{\text{loss,fluid}} = \dot{V}\Delta p_{\text{t}}$ (where $\dot{V}$ is the volumetric flow rate). By this estimation, the HP, HF case shows a 96.3% reduction in $P_{\text{loss,fluid}}$ from the LP, HF case. This indicates that the high-pressure air receiver experiences a significantly lower pumping loss for comparable thermal performance.[5] The pumping loss for all cases is less than 10% of the heat transfer rate. For an estimation of receiver thermal performance in context with pressure losses integrated into a Brayton cycle, the reader is referred to [28].

Table 5 further shows that the peak von Mises stress is much larger for the high-pressure cases; it also marginally increases with mass flow rate as a consequence of the tension caused by the fluid-body force. The effect of a ×4 dimensional up-scale was explored for the LP, LF case (because this case can afford the additional mechanical stress). As shown in the table: the mass flow rate and the output thermal power increase by almost $\times 4^2$ to reach the same outlet temperature. However, the thermal efficiency decreases with a corresponding increase in exterior surface temperature.

6. Conclusion

A new pressurized air receiver concept has been explored based on the novel Tadpole heat transfer device. In an investigation on dimensional scaling, it was found that the scaling of the receiver's heat transfer units is sensitive to material stress and the constraint of a thin

[5] It must be noted that the adiabatic and incompressibility assumptions cause a large uncertainty. The average density was used for calculating $\dot{V}$ through mass conservation. An uncertainty of 36.3% is expected, attributed to the density variation (peak to average) through the domain. Because the relative error applies similarly for the compared cases, the comparison is deemed to hold for a rough estimation of power loss improvement.

outer-shell thickness does not permit a large internal volume for the units. Scaling the receiver for a desired thermal rating can be achieved by modifying the number of heat transfer units along with the aperture size.

A Heliopod heliostat field was developed that makes use of an aiming strategy to produce a relatively uniform flux distribution on the receiver aperture. The resulting flux distribution was projected on the external 3D surface of a central heat transfer unit and translated to a volumetric heat source boundary condition for the 3D Computational Fluid Dynamics model. The model considers convective heat transfer and radiative heat losses. Natural-convective heat losses are estimated with a correlation. An assumption is also made for reflective losses.

The receiver concept's capability to reach an outlet temperature of 800 °C was estimated at various operating conditions. The initial outlook estimated a thermal efficiency of 59.3% and a total pressure loss of 0.564 kPa for an outlet temperature of 801 °C under a flux of 635 kW/m^2. A material temperature of above 1000 °C was simulated. The performance of a high-pressure operating condition was compared to a low-pressure operating condition. Similar thermal efficiencies were estimated; although it was estimated that the low-pressure case exhibits significantly increased pumping losses. The receiver demonstrates higher thermal efficiencies at a lower aperture flux level of between 635 kW/m^2 and 1270 kW/m^2 instead of a high flux of 2530 kW/m^2.

It was found that a large internal heat transfer coefficient characteristic of an impinging jet or a Tadpole is not sufficient on its own to achieve the high outlet temperatures required in a receiver for application in a Concentrating Solar Power plant. Instead, the ratio of exterior surface area to the aperture area of a receiver must also be maximized to enable absorbing a large aperture flux, achieve a high outlet temperature with a safe absorber temperature and a competitive thermal efficiency. This should be combined with a semi-enclosed cavity to limit radiative and convective heat losses. The limitation of the heat transfer fluid and its energy density should also be considered. The limitation of the concept may be overcome by taking advantage of larger surface area ratios such as the SCRAP and SOLUGAS concepts. To achieve the allowable temperature limits, further iteration can be performed for a modified design exploiting a larger surface area using the method followed here to evaluate the concept.

Declaration of competing interest

The authors declare the following financial interests/personal relationships which may be considered as potential competing interests: Derwalt Johannes Erasmus reports financial support was provided by Stellenbosch University.

Data availability

Data will be made available on request.

Acknowledgements

This work was made possible by an Erasmus+ mobility grant awarded by Alliance4Universities which made a collaboration at UC3M possible. The continued support of the Solar Thermal Energy Research Group (STERG) is appreciated. The South African centre for high performance computing (CHPC) is acknowledged for providing computational resources.

References

[1] W. Lipiński, E. Abbasi-Shavazi, J. Chen, J. Coventry, M. Hangi, S. Iyer, A. Kumar, L. Li, S. Li, J. Pye, J.F. Torres, B. Wang, Y. Wang, V.M. Wheeler, Progress in heat transfer research for high-temperature solar thermal applications, Appl. Therm. Eng. 184 (2021) 116137, URL http://dx.doi.org/10.1016/j.applthermaleng.2020.116137.

[2] D.G. Kröger, SUNSPOT — The Stellenbosch UNiversity Solar POwer Thermodynamic cycle, Technical Report, Stellenbosch University, 2012, URL https://sterg.sun.ac.za/wp-content/uploads/2011/05/SUNSPOT-2.pdf. (Date accessed: January 2021).

[3] L. Heller, P. Gauché, Modeling of the rock bed thermal energy storage system of a combined cycle solar thermal power plant in South Africa, Sol. Energy 93 (2013) 345–356, URL http://dx.doi.org/10.1016/j.solener.2013.04.018.

[4] R. Korzynietz, J.A. Brioso, A. Del Río, M. Quero, M. Gallas, R. Uhlig, M. Ebert, R. Buck, D. Teraji, Solugas — Comprehensive analysis of the solar hybrid Brayton plant, Sol. Energy 135 (2016) 578–589, URL http://dx.doi.org/10.1016/j.solener.2016.06.020.

[5] P. Gauché, T.W. Von Backström, A.C. Brent, J. Rudman, CSP opportunity and challenges in a national system: The WWF renewable vision for a 2030 South African electricity mix, in: AIP Conference Proceedings, SolarPACES 2015, vol. 1734, (1) Cape Town, 2016, 080002, URL https://aip.scitation.org/doi/abs/10.1063/1.4949182.

[6] P. Doron, A high temperature receiver for a solarized micro-gas-turbine, in: AIP Conference Proceedings, SolarPACES 2019, vol. 2303, (030012) Daegu, 2020, URL https://aip.scitation.org/doi/abs/10.1063/5.0028527.

[7] M. Lubkoll, Performance characteristics of the Spiky Central Receiver Air Preheater (SCRAP) (Ph.D. thesis), (March) Stellenbosch University, South Africa, 2017, URL http://hdl.handle.net/10019.1/101295.

[8] H. Saravanamuttoo, G.F.C. Rogers, H. Cohen, Gas Turbine Theory, fifth ed., Pearson Education, Upper Saddle River, United States, 2001.

[9] H.-J. Lee, J.-K. Kim, S.-N. Lee, H.-K. Yoon, Y.-H. Kang, M.-H. Park, Calculation of optical efficiency for the first central-receiver solar concentrator system in Korea, Energy Procedia 69 (2015) 126–131, URL http://dx.doi.org/10.1016/j.egypro.2015.03.015. International Conference on Concentrating Solar Power and Chemical Energy Systems, SolarPACES 2014.

[10] X. Rández, F. Zaversky, D. Astrain, A novel active volumetric rotating disks solar receiver for concentrated solar power generation, Appl. Therm. Eng. 206 (2022) 118114, URL http://dx.doi.org/10.1016/j.applthermaleng.2022.118114.

[11] Y. Shuai, B. Guene Lougou, H. Zhang, D. Han, B. Jiang, J. Zhao, X. Huang, Combined heat and mass transfer analysis of solar reactor integrating porous reacting media for water and carbon dioxide splitting, Sol. Energy 242 (2022) 130–142, URL http://dx.doi.org/10.1016/j.solener.2022.07.017.

[12] K. Allen, T.W. Von Backström, E. Joubert, P. Gauché, Rock bed thermal storage: Concepts and costs, in: AIP Conference Proceedings, SolarPACES 2015, 1734, (1) Cape Town, 2016, 050003, URL https://aip.scitation.org/doi/pdf/10.1063/1.4949101.

[13] T. Neises, C. Turchi, A comparison of supercritical carbon dioxide power cycle configurations with an emphasis on CSP applications, Energy Procedia 49 (2014) 1187–1196, URL http://dx.doi.org/10.1016/j.egypro.2014.03.128. Proceedings of the SolarPACES 2013 International Conference.

[14] R.W. Swindeman, D.L. Marriott, Criteria for design with structural materials in combined-cycle applications above 815 °F, Trans. ASME, J. Eng. Gas Turbines Power 116 (2) (1994) 352–359, URL http://dx.doi.org/10.1115/1.2906827.

[15] P. González-Gómez, M. Rodríguez-Sánchez, M. Laporte-Azcué, D. Santana, Calculating molten-salt central-receiver lifetime under creep-fatigue damage, Sol. Energy 213 (2021) 180–197, URL http://dx.doi.org/10.1016/j.solener.2020.11.033.

[16] M. Mcmurtrey, R. Rupp, B. Barua, M. Messner, Creep-fatigue Behavior and Damage Accumulation of a Candidate Structural Material for Concentrating Solar Power Solar Thermal Receiver (Final Technical Report), 2021, URL http://dx.doi.org/10.2172/1797935.

[17] Z. Panchbhaya, Numerical investigation of heat transfer enhancement in solar receiver tubes Master's thesis, Stellenbosch University, South Africa, 2020, URL http://hdl.handle.net/10019.1/108308.

[18] Y.C. Soo Too, R. Benito, Enhancing heat transfer in air tubular absorbers for concentrated solar thermal applications, Appl. Therm. Eng. 50 (1) (2013) 1076–1083, URL http://dx.doi.org/10.1016/j.applthermaleng.2012.06.025.

[19] K.J. Craig, M. Slootweg, J.P. Meyer, J.C. Robbins, R. Kotzé, N.J.M. Honiball, E. Grobler, T.J. Oosthuizen, W. Winterbach, CFD simulation of solar receiver jet impingement heat transfer: Rans vs LES, in: 16th International Heat Transfer Conference, vol. 16, (23262) 2018, pp. 1971–1978, URL http://dx.doi.org/10.1615/IHTC16.cms.023262.

[20] O. Garbrecht, F. Al-sibai, R. Kneer, K. Wieghardt, Numerical investigation of a new molten salt central receiver design, in: SolarPACES 2012, Marrakech, 2012.

[21] K.J. Craig, M. Slootweg, J.P. Meyer, Heat transfer enhancement in molten salt central receiver using jet impingement, in: 5th Southern African Solar Energy Conference, SASEC, vol. 5, Durban, South Africa., 2018, URL https://www.sasec.org.za/full_papers/53.pdf. (Date accessed: October 2020).

[22] J. Quick, Computational investigation of swirling jet impingement in a concentrated solar tower receiver Master's thesis, University of Pretoria, South Africa, 2021, URL https://repository.up.ac.za/handle/2263/85249.
[23] W. Wang, B. Laumert, H. Xu, T. Strand, Conjugate heat transfer analysis of an impinging receiver design for a dish-Brayton system, Sol. Energy 119 (2015) 298–309, URL http://dx.doi.org/10.1016/j.solener.2015.07.013.
[24] L. Li, Numerical study of surface heat transfer enhancement in an impinging solar receiver Master's thesis, Uppsala University, 2014, URL http://urn.kb.se/resolve?urn=urn:nbn:se:uu:diva-237365. (Date accessed: October 2020).
[25] W. Wang, B. Laumert, An axial type impinging receiver, Energy 162 (2018) 318–334, URL http://dx.doi.org/10.1016/j.energy.2018.08.036.
[26] M. Lubkoll, D.J. Erasmus, T.M. Harms, T.W. Von Backström, D.G. Kröger, Performance characteristics of the spiky central receiver air pre-heater (SCRAP), Sol. Energy 201 (2020) 773–786, URL http://dx.doi.org/10.1016/j.solener.2020.03.027.
[27] D.J. Erasmus, M. Lubkoll, K.J. Craig, T.W. von Backström, Impingement heat transfer with pressure recovery, Heat Mass Transf. 58 (2022) 1857–1875, URL http://dx.doi.org/10.1007/s00231-022-03186-2.
[28] D. Erasmus, The Development of a Novel Impingement Heat Transfer Device, Master's thesis, Stellenbosch University, South Africa, 2020, URL https://scholar.sun.ac.za/handle/10019.1/109296.
[29] R. Pérez-Álvarez, P.Á. González-Gómez, A. Acosta-Iborra, D. Santana, Thermal stress and fatigue damage of central receiver tubes during their preheating, Appl. Therm. Eng. 195 (2021) 117115, URL http://dx.doi.org/10.1016/j.applthermaleng.2021.117115.
[30] N. Dowling, Mechanical Behavior of Materials: Engineering Methods for Deformation, Fracture, and Fatigue, fourth ed., Pearson Prentice Hall, USA, 2013.
[31] D.G. Kröger, Spiky Central Receiver Air Pre-heater (SCRAP), Technical Report, Stellenbosch University, 2008, pp. 1–3.
[32] SMC, Inconel Alloy 718, (SMC-045) Special Metals Corporation, Huntington, USA, 2007.
[33] W. Wu, R. Uhlig, R. Buck, R. Pitz-Paal, Numerical simulation of a centrifugal particle receiver for high-temperature concentrating solar applications, Numer. Heat Transfer A 68 (2) (2015) 133–149, URL http://dx.doi.org/10.1080/10407782.2014.977144.
[34] D.G. Kröger, Air-Cooled Heat Exchangers and Cooling Towers, first ed., Stellenbosch University, South Africa, 2004.
[35] A. Sánchez-González, D. Santana, Solar flux distribution on central receivers: A projection method from analytic function, Renew. Energy 74 (2015) 576–587, URL http://dx.doi.org/10.1016/j.renene.2014.08.016.
[36] Z.D. Cheng, Y.L. He, F.Q. Cui, Numerical investigations on coupled heat transfer and synthetical performance of a pressurized volumetric receiver with MCRT-FVM method, Appl. Therm. Eng. 50 (1) (2013) 1044–1054, URL https://10.1016/j.applthermaleng.2012.08.045.
[37] M. Slootweg, K.J. Craig, J.P. Meyer, Investigation into central receiver design for optimal optical and thermal performance, in: 5th Southern African Solar Energy Conference, SASEC, Durban, South Africa, 2018, URL https://www.sasec.org.za/full_papers/54.pdf. (Date accessed: October 2020).
[38] A. Sánchez-González, M.R. Rodríguez-Sánchez, D. Santana, FluxSPT: Tool for heliostat field aiming and flux mapping in solar power tower plants, in: AIP Conference Proceedings, SolarPACES 2020, vol. 2445, 2022, 120020, Online conference. URL https://doi.org/10.1063/5.0085656.
[39] C.-A. Domínguez-Bravo, S.-J. Bode, G. Heiming, P. Richter, E. Carrizosa, E. Fernández-Cara, M. Frank, P. Gauché, Field-design optimization with triangular heliostat pods, in: AIP Conference Proceedings, SolarPACES 2015, vol. 1734, (1) Cape Town, 2016, 070006, URL https://aip.scitation.org/doi/abs/10.1063/1.4949153.
[40] A. Sánchez-González, M.R. Rodríguez-Sánchez, D. Santana, Aiming factor to flatten the flux distribution on cylindrical receivers, Energy 153 (2018) 113–125, URL http://dx.doi.org/10.1016/j.energy.2018.04.002.
[41] W.A. Landman, Optical performance of the reflective surface profile of a heliostat (Ph.D. thesis), Stellenbosch University, South Africa, 2017, URL http://scholar.sun.ac.za/handle/10019.1/101210.
[42] D.J. Erasmus, A. Sánchez-González, T.W. Von Backström, Blossaim, a deterministic aiming strategy for circular aperture receivers, in: AIP Conference Proceedings, SolarPACES 2020, vol. 2445, 2022, 120012, Online conference. URL https://aip.scitation.org/doi/abs/10.1063/5.0085654.
[43] VDI, VDI-Wärmeatlas, 10. Auflag ed., Springer-Verlag Berlin Heidelberg, Germany, 2010.
[44] G. Greene, C. Finfrock, T. Irvine, Total hemispherical emissivity of oxidized inconel 718 in the temperature range 300c–1000c, Exp. Therm Fluid Sci. 22 (3–4) (2000) 145–153, http://dx.doi.org/10.1016/S0894-1777(00)00021-2.
[45] J. Garrido, L. Aichmayer, A. Abou-Taouk, B. Laumert, Experimental and numerical performance analyses of Dish-Stirling cavity receivers: Radiative property study and design, Energy 169 (2019) 478–488, URL http://dx.doi.org/10.1016/j.energy.2018.12.033.
[46] M. Slootweg, K.J. Craig, J.P. Meyer, A computational approach to simulate the optical and thermal performance of a novel complex geometry solar tower molten salt cavity receiver, Sol. Energy 187 (2019) 13–29, URL http://dx.doi.org/10.1016/j.solener.2019.05.003.
[47] K. Craig, M. Slootweg, W. Le Roux, T. Wolff, J. Meyer, Using CFD and ray tracing to estimate the heat losses of a tubular cavity dish receiver for different inclination angles, Sol. Energy 211 (2020) 1137–1158, URL http://dx.doi.org/10.1016/j.solener.2020.10.054.
[48] D.L. Siebers, J.S. Kraabel, Estimating convective energy losses from solar central receivers, Technical Report, (SAND-84-8717) Sandia National Laboratories, Albuquerque, New Mexico., 1984, URL http://dx.doi.org/10.2172/6906848.
[49] Y.A. Çengel, J.M. Cymbala, Fluid Mechanics Fundamentals and Applications, third ed., McGraw-Hill, New York, USA, 2014.